J MATER RES TECHNOL. 2020;9(2):1708–1719

Available online at www.sciencedirect.com

jmr&t
Journal of Materials Research and Technology
www.jmrt.com.br

Original Article

Plastic flow behavior of twinning induced plasticity steel from low to warm temperatures

Manuela De Maddis[*], *Pasquale Russo Spena*

Department of Management and Production Engineering, Politecnico di Torino, Corso Duca degli Abruzzi 24, 10129 Torino, Italy

ARTICLE INFO

Article history:
Received 10 October 2019
Accepted 30 November 2019
Available online 19 December 2019

Keywords:
Twinning induced plasticity steel
Plastic flow behavior
Warm temperature
Mechanical strength
Strain hardening
Dynamic strain aging

ABSTRACT

This work investigates the tensile behavior of twinning induced plasticity (TWIP) steel under room to warm temperatures. Stress-strain flow curves have been obtained from steady-state uniaxial tensile tests performed at different temperatures, that is, from 20 to 800 °C, and different engineering strain rates, 0.003 and 0.5 s^{-1}. The yield and ultimate tensile strength, elongation at fracture, reduction of area, strain hardening exponent and strain hardening rate have been defined to describe the plastic behavior of TWIP steel. It has been found that the plastic flow behavior of TWIP steel is characterized by negative strain rate sensitivity and strain hardening, at temperatures from 20 to 300 °C, until the twinning mechanism occurs. At these temperatures, dynamic strain aging starts at the beginning of plastic deformation, with the appearance of fluctuations in the work hardening rate and local strain rate. Pronounced local serrations also appear at 300 °C and 0.003 s^{-1}. Plastic deformation is mainly driven by dislocation gliding at 550 and 800 °C, and mechanical twins are absent. As a result, negative strain rate sensitivity and local serrations disappear in the stress-strain curves. Creep also contributes notably to plastic deformation at 800 °C, as was also observed on the fracture surfaces of tensile samples. Mechanical twins were only visible for the lower temperatures. The grains in the sample tested at 800 °C and 0.003 s^{-1} were fully recrystallized.

1. Introduction

Over the last decade, several steelworks have proposed new advanced high strength steels (AHSSs) to the automotive industry for several purposes, including the reduction of vehicle weight, car safety (i.e. crashworthiness) and passenger comfort improvements, and the reduction of greenhouse emissions and fuel consumption. Various AHSS grades are currently employed to produce car body parts, including dual phase (DP), transformation induced plasticity (TRIP) and hot stamping boron steels. The current stringent environmental regulations continue to drive the evolution of AHSSs toward steel grades with more and more impressive combinations of strength and ductility. Recent studies have been aimed at investigating the use of twinning induced plasticity (TWIP) steels for the fabrication of vehicle components, due to their outstanding mechanical properties. TWIP are austenitic steels with variable carbon (0.05-0.60 wt.%) and manganese (10–25 wt.%) contents. The ultimate tensile strength of TWIP steel generally exceeds 900 MPa, and they have total elongations of over 40 % [1–6]. Studies have demonstrated that

---

[*] *Corresponding author.*
E-mail: manuela.demaddis@polito.it (M. De Maddis).

https://doi.org/10.1016/j.jmrt.2019.11.094

twinning and dynamic strain aging (DSA) contribute to the observed high strain hardening, and hence to the excellent mechanical properties of TWIP steel [7]. However, their use in the automotive industry is currently restricted to prototypes and to a very few uncoated structural components. This is mainly due to some issues that have arisen related to the fabrication of zinc-coated TWIP sheets, dissimilar welding and liquid metal embrittlement [8,9]. However, promising TWIP steel developments are underway and many recent studies have concerned sheet forming and welding [10–16].

The computation of energy/power consumption for industrial sheet metalworking and of the mechanical loads requires a comprehensive analysis of the flow behavior (e.g., flow stress and strain hardening rate) of steel sheets during plastic deformation [17–19]. This is of utmost importance when sheet forming operations are carried out at low and warm temperatures since the mechanical stresses in dies and sheets are normally more powerful than those that occur during hot forming. In addition, optimized forming operations can be pursued by means of accurate knowledge of the elastoplastic behavior of the metals until failure. Steady-state uniaxial tensile tests are commonly carried out for both low and high strain rate characterization of metal sheets. In this regard, strain hardening by dislocations, austenite-to-ε-martensite transformation, mechanical twinning, dynamic strain aging (DSA), or a combination of them are all possible strain hardening mechanisms of TWIP steels. Each of these mechanisms can or cannot be dominant in influencing the plastic flow behavior of TWIP steels based on steel chemical composition, strain, strain rate, temperature, and grain size. Strain hardening by dislocations is the most common and studied strengthening mechanism in metals. As well known, dislocation density increases dramatically during plastic deformation. The ensuing reduction of the mean free path of dislocations due to the increase number of dislocations (e.g., Frank-Read and Orowan mechanisms) and to the reduction of grain size leads to strain hardening [20,21].

Mechanical twinning and austenite-to-ε-martensite transformation contribute to the high strain hardening of TWIP steels because twin boundaries act as obstacles to dislocation glide through a dynamic Hall-Petch effect [22,23]. The extent of mechanical twinning and austenite-to-ε-martensite transformation during plastic deformation is primarily driven by stacking fault energy (SFE) [24–30]. TWIP steel with an SFE of less than 20 mJ/m^2 deforms as a result of a combination of dislocation gliding and austenite-to-ε-martensite transformation. For intermediate SFE values in the 20−50 mJ/m^2 range, the austenite-to -ε-martensite transformation is replaced by mechanical twinning, which contributes to plastic deformation through dislocation gliding. When the SFE is increased to over 50 mJ/m^2, plastic deformation is caused principally by dislocation gliding. Dislocation gliding and SFE are thermally dependent phenomena: increases in temperature increase SFE and, hence, the tendency of dislocation gliding and austenite-to-ε-martensite transformation during plastic deformation. In addition, increases in temperature enhance the activation of other glide planes, dislocation climbing, and cross-slip. The strain rate also influences the competition between mechanical twinning, dislocation gliding and austenite-to-ε-martensite transformation. The strain rate, in particular, enhances dislocation gliding. The effects of the temperature and strain rate are generally coupled with an Arrhenius relationship [31]. DSA is another strain hardening mechanism that can concur with the metal hardening of TWIP steels. It is based on the interaction between mobile dislocations and diffusing solute atoms during plastic deformation. According to Rose and Glover [32] and other studies [33–35], the presence of C and N interstitial elements are fundamental in causing DSA. Interstitial atoms are attracted by dislocations because they lower dislocation energy, thus higher stress is required to free dislocations. When dislocations pin at obstacles (e.g. precipitates, forests of dislocations) during gliding, they undergo an additional pin due to interstitial atom diffusion. Under sufficient stress, dislocations will overcome these obstacles and will move through the crystal lattice up to they will again be pinned by obstacles or by diffusing solutes. Dislocations again stop and the process can repeat. This is why this strain hardening mechanism is often referred to as dynamic strain aging. In manganese steels, like TWIP grade, the interplay between Mn and C atoms also promotes the occurrence of Mn-C clusters that firmly pin dislocations through their fast re-orientation at the core of moving dislocations [36]. Lüders bands and the Portevin–Le Chatelier effect are the most well-known macroscopic manifestations of DSA, even though this mechanism is known to affect metals without these physical observations. Since DSA is primarily based on the interactions between dislocations and diffusing solute atoms, this phenomenon is highly dependent on strain rate and temperature.

A better understanding of the plastic flow behavior of TWIP steel for different strain rates and for temperatures ranging from low to warm could be beneficial for the use of this steel grade in the sheet forming of lightweight and high resistant automotive parts, even those with complex geometries. Steel components normally experience a wide range of strain rates during sheet forming operations, most of which can be reproduced by means of tensile tests with strain rates ranging from quasi-static to 0.5 s^{-1}. In this regard, the aim of this study has been to investigate the plastic flow behavior of TWIP steel through steady-state uniaxial tensile tests, which were executed on flat dog-bone specimens. Tensile samples were subjected to plastic deformations at temperatures ranging from 20 to 800 °C and at different strain rates, that is, 0.003 and 0.5 s^{-1}. The tensile behavior was determined for the different testing conditions in terms of yield and ultimate tensile strength, elongation at fracture, reduction of area, strain hardening exponent and strain hardening rate. The microstructures of the tensile samples were also assessed after mechanical testing, both at a distance from and close to the necking region. The fracture mode of the samples was also determined.

2. Materials and methods

Industrial TWIP steel sheets, with a thickness of 1.4 ± 0.05 mm, have been used to assess the plastic flow behavior at temperatures ranging from low to warm. The chemical composition of the sheets, as measured by means of optical emission spectroscopy, is listed in Table 1. The SFE of the TWIP steel was

Table 1 – Chemical composition (%wt.) of TWIP steel, as measured by means of optical emission spectroscopy, and the estimated SFE according to Pierce et al. [27].

Steel	%C	%Si	%Mn	%P + S	%Al	%Nb	%Ti	%V	%Fe	SFE [mJ/m^2]
TWIP	0.51	0.13	15.0	<0.02	1.00	0.009	0.003	0.10	bal.	30 ± 10

Table 2 – Average mechanical properties and grain size of TWIP steel. YS: yield strength; UTS: ultimate tensile strength; e_f: elongation at fracture.

Steel	YS [MPa]	UTS [MPa]	e_f [%]	Hardness [HV1]	Average grain size [μm]
TWIP	540	1030	52	240	7

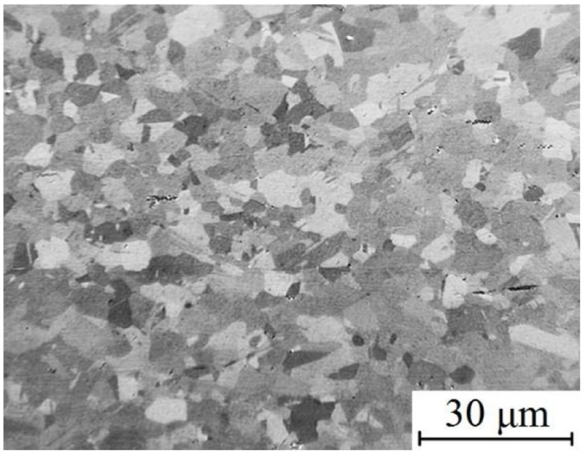

Fig. 1 – Optical micrograph of TWIP steel (Le Pera etching).

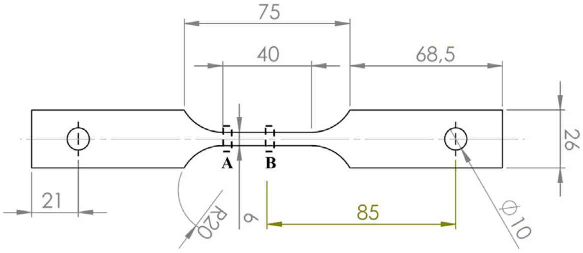

Fig. 2 – Drawing of the tensile samples (sub-size specimen according to the ASTM E8 standard) subjected to tensile tests for various temperatures and strain rates. Sampling positions for the SEM microstructural examinations: at the border of the gauge region, A; at the fracture surface, B.

computed according to the work of Pierce et al. on the SFE energy of Fe-Mn-C-Al TWIP steels [27]. In that study, the examined TWIP steel had an SFE of 30 ± 10 mJ/m^2. Therefore, plastic deformation should be driven above all by a combination of dislocation gliding and mechanical twinning.

The main mechanical properties and the microstructure of the TWIP sheets are reported in Table 2 and Fig. 1, respectively. The tensile properties at room temperature were assessed according to ASTM E8 [37], whereas the tensile properties at high temperatures were assessed based on the ASTM E21 standard [38]. Strain hardening was established on the basis of the ASTM E646 [39] standard. All the data reported hereafter are the averages of at least three distinct testing repetitions.

Pin-loaded tension specimens were fabricated from TWIP sheets by laser cutting, see Fig. 2. The cut surfaces of the samples were then finished by milling to attain an appropriate surface roughness.

Steady-state uniaxial tension tests were performed with an MTS machine, mod. C45, equipped with a 100 kN load cell. A cylindrical heating furnace, see Fig. 3, was used to heat the samples. The furnace had a temperature controller with two R-type thermocouples placed on the ends of the gauge length to measure the specimen temperature. For the duration of the test (defined as the time from the application of force until fracture), it was always verified that the difference between the temperature indicated by the thermocouples and the nominal test temperature did not exceed ±3 °C, which is the permitted temperature variation for tensile testing under 1000 °C according to ASTM E21 standard. A ceramic insulator was used on the thermocouples in the hot zone to avoid thermal interferences from the surrounding environment. A high-temperature extensometer, with a gage length of 25 mm, was used to measure sample elongation. Specimens were tested with the tensile axis parallel to the rolling direction and from low to warm conditions at four temperatures of 20, 300, 550 and 800 °C, considering two strain rates of 0.003 and 0.5 s^{-1}. The rate of heating of the sample was set at 0.2 °C/s to ensure a gradual increase in temperature of the sample and reduce a possible thermal gradient between the furnace and the sample. The temperature measured on the sample surface drove the heat developed by the furnace to ensure the set rate of heating of the sample. The specimens were soaked for 1 min before the tensile test to ensure full temperature homogenization throughout the gage volume. Preliminary tensile tests, which were carried out by the authors, demonstrated that this soaking time was sufficient to homogenize the temperature inside the samples. In this regard, no differences in both the microstructure and tensile curves were detected between the samples soaked for 1 min and 20 min (the latter recommended by ASTM E21 standard). Therefore, the small heating rate and specimen size ensured homogeneous heating of the samples with the possibility to reduce the soaking time. At the end of the test, the samples were immediately cooled to room temperature to preserve their microstructure and limit grain recrystallization. The final cooling to room temperature consisted of opening rapidly the furnace and then blowing argon gas, from a tank, on tensile specimens. The tensile data were collected at a sampling rate of 50 Hz. The testing schedules are schematically illustrated in Fig. 4. At least three tensile tests were performed for each testing condition to have consistent results.

Metallographic samples were extracted from the ends of the fractured specimens along the tensile direction. These samples were then hot mounted and polished by means of

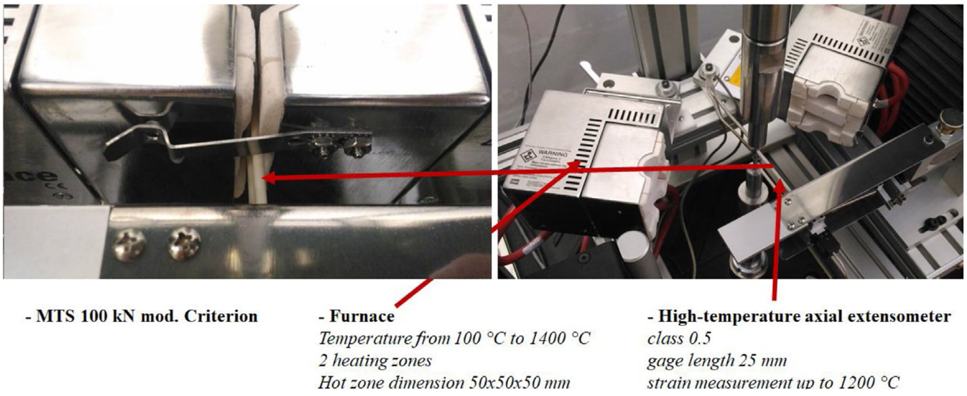

Fig. 3 – Equipment used to perform the tensile tests for various temperatures and strain rates.

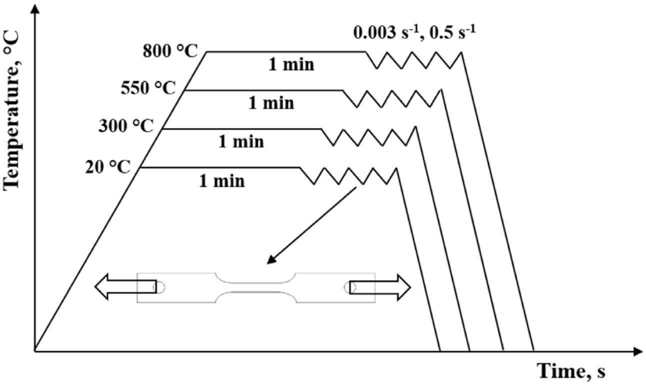

Fig. 4 – Schematic of the tensile test schedules used to assess the plastic flow behavior of TWIP steel for various temperatures and strain rates. The graph is not to scale.

mechanical grinding with SiC paper and a 0.25 μm diamond polishing solution. Finally, the specimens were etched with a 10 %vol. of nitric acid in methanol for 20 s. The microstructure of the tensile specimens was examined by means of scanning electron microscopy (SEM). The ductility of the specimens was measured, by means of an optical microscope, as the reduction of the transverse area. The tensile sample fracture modes were assessed through an SEM examination of the fractured surfaces.

3. Results

3.1. *Plastic flow behavior*

The design of AHSS sheet components involves reducing and postponing plastic instability, i.e. local necking, during sheet forming operations. In a tensile test, this means maximizing the uniform elongation evaluated at the peak load. The onset of instability can theoretically be assessed using the Considère criterion: instability occurs when the slope of the true stress-strain curve is equal to the true stress. The engineering and true stress-strain curves of TWIP steel are displayed in Fig. 5a and b, respectively, for various test conditions. The strain hardening exponent, n, was computed according to the Hollomon relationship $\sigma = K\varepsilon^n$, to assess the hardening capability of TWIP steel during plastic deformation. The strain hardening values are reported in Fig. 5b, less the true curves obtained at 800 °C and 0.5 s^{-1}, because of the absence of strain hardening. The true stress-strain curves were calculated from the engineering stress-strain curves up to necking. It was not possible to directly evaluate the true stress-strain curves after the beginning of necking (as a reduction of the area of the necking region) because the samples were inside the furnace during the test. The uniform elongation and ultimate tensile strength were obtained from the plastic instability condition on the basis of the Considère criterion. The yield strength was evaluated as 0.2 % proof stress, while the elongation at fracture was evaluated as the final point of the engineering stress-strain curve. Fig. 6 summarizes the main tensile properties in terms of yield and tensile strength, elongation at fracture and uniform elongation.

Regardless of the strain rate, it has been shown that the yield and ultimate tensile strength of TWIP steel are in the 150–700 MPa and 150–1050 MPa ranges, respectively, when the tested temperature goes from room temperature to 800 °C. Fracture elongation ranges approximately from 30 to 55 %. The product of fracture elongation and tensile strength at room temperature is in the 50–55 GPa% range, which points out the remarkable energy absorption capacity of TWIP steel.

Yield and ultimate tensile strength reduce as the temperature is increased, whereas the effect of the strain rate on the flow behavior is more complex for varying temperatures. For all the examined testing temperatures, the strain rate increases the yield strength. This is the result of the well-known effect of the strain rate on reducing the initial moving capability of dislocations at the beginning of plastic deformation. Strain rate has instead an opposite effect on strain hardening of TWIP steel when tested at lower and higher temperatures. At 20 and 300 °C, strain hardening reduces with the increase in the strain rate, as shown in Fig. 5b. This is because the examined TWIP steel exhibits negative strain rate sensitivity (also known as strain rate softening) in this range of temperature [1–3]. This result is in agreement with previous studies carried out on Fe-C-Mn steels [40–42]. The opposite effects of strain rate on yield point (driven by dislocation glide) and on work hardening (driven by twinning and DSA) lead to an intersection of the tensile curves obtained at 20 and

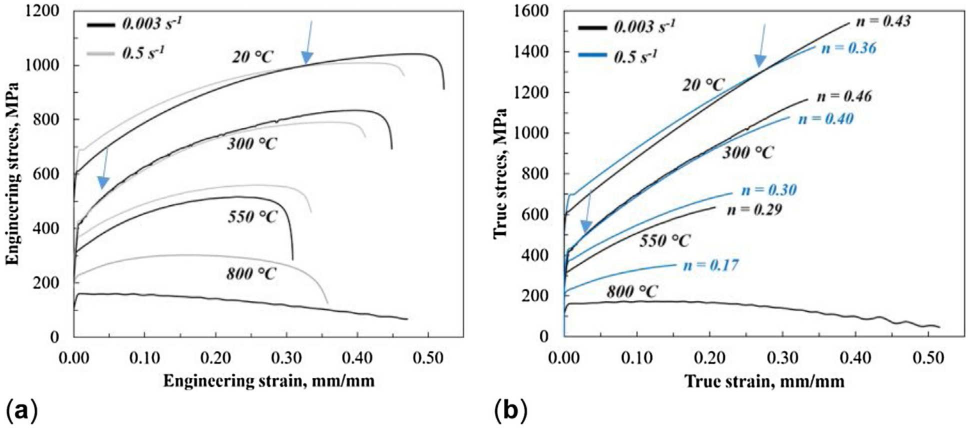

Fig. 5 – (a) Engineering and (b) true stress-strain curves and strain hardening exponent (n-value) for various temperatures and strain rates. Arrows highlight the intersections of the tensile curves.

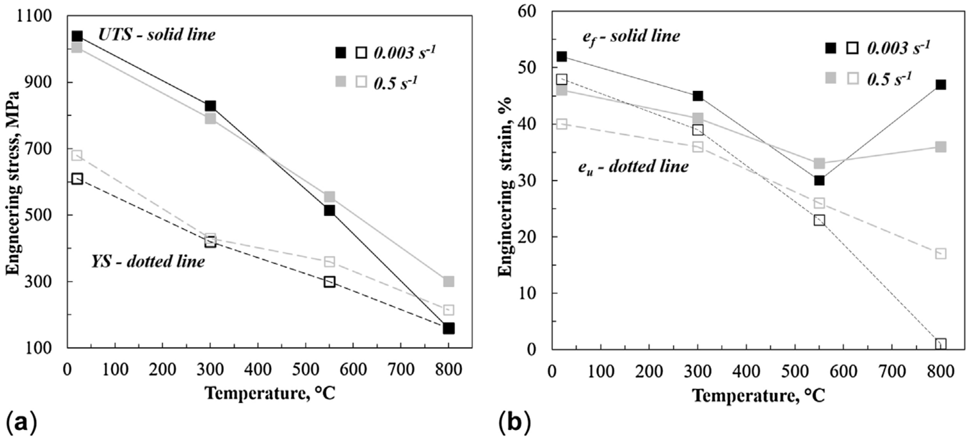

Fig. 6 – Tensile properties for the various test conditions: (a) Ultimate tensile strength (UTS) and yield strength (YS); (b) uniform elongation (e_u) and elongation at fracture (e_f).

300 °C. That is, the high strain rate increases the yield point, but reduces strain hardening capability and hence the slope of the tensile curve. The intersection of tensile curves is pointed out by the arrows in Fig. 5a and b.

Strain hardening reduces to a great extent in the samples tested at 550 and 800 °C. In addition, negative strain rate sensitivity disappears, thus strength hardening increases with an increase of strain rate. This different plastic behavior of TWIP steel is attributed to the effect of temperature on mechanical twinning and DSA. An increase in temperature increases SFE, which reduces twinning of the crystal lattice. Moreover, temperature actives several slip systems, enhances dislocation climbing and cross-slip, as well as the motility of Fe atoms. All these phenomena prevent continuous pinning of dislocations by solute clusters, thereby mitigating DSA. As a result, plastic behavior is mainly driven by dislocation gliding and thermally-assisted phenomena at higher temperatures, with the strain hardening exponent that reduces continuously according to the predominant effect of dislocation gliding. Fig. 5 shows how the yield and tensile strength increase as the strain rate increases and the reduction of strain hardening exponent when samples are tested at 550–800 °C. Creep has also a primary effect on TWIP deformation at 800 °C for the lowest strain rate: the stress-strain curve shows a stress peak at the beginning of deformation, which is then followed by a continuous reduction in stress to the final fracturing. The final waving visible at the end of the stress curves at 800 °C is attributable to the fact that the testing equipment is unable to maintain a constant strain rate in a sample with a cross-section that reduces to a very small area. In this test condition, the fractured area was evaluated as 0.5 mm^2 or less. Regardless of the strain rate value, the engineering stress-strain curves show that necking occurs close to the final fracture (i.e. fracturing occurs after a short elongation and after the onset of necking) in the samples tested up to 500 °C. This is a normal behavior of TWIP steels, and it is due to their high strain hardening, which postpones the onset of necking to high strains.

When samples are subjected to high strain rates during tensile tests, the plastic deformation approaches to an adiabatic condition, that is, a large amount of deformation work is converted into heat. This condition leads to a rise in temperature sample and, in turn, to thermal softening. In such a situation, the resulting flow stress is lower than the actual flow stress under an isothermal condition. Based on the work of Madivala and Bleck [43] on the strain rate effect of mechanical properties of TWIP steel, a strain rate up to 0.5 s^{-1} may cause an increase of temperature up to 100 °C at the point of fracture. Such a rise in temperature led to an increase of SFE, thereby reducing twinning behavior in favor of dislocation glide. Therefore, it can be assumed that a thermal softening might occur for the samples tested at 0.5 s^{-1}. However, the thermal softening at this level of strain rate influences the flow stress of TWIP steel less than the strain rate, becoming more and more irrelevant with the rise in temperature, and hence for 300, 550, and 800 °C test conditions.

In Fig. 7, it can be observed that the stress-strain curves show serrations at 20 and 300 °C under 0.003 s^{-1}. These serrations are associated with a delta stress value (i.e. extent of the serrations in terms of stress) of 5–10 MPa. They are quite small as compared to previous studies that found serrations associated with delta stress values of 50 MPa and over [1,42]. These serrations, which are also known as jerky flows or serrated flows, have been described in terms of the Portevin-Le-Chatelier (PLC) effect [1,33,44–47]. This effect is associated with DSA. Serrations are the macroscopic result of the continuous and alternate pinning and unpinning of dislocations from interstitial elements.

PLC behavior and the serrations of TWIP steel depend to a great extent on several factors, including the chemical composition, grain size, temperature and strain rate of the steel. Some studies [48] have pointed out that the strain hardening process consists of different steps: 1) the beginning of plastic deformation due to dislocation gliding; ii) dislocation interaction and the consequent activation of deformation mechanisms through twinning; iii) the progression of deformation without serrations; iv) the progression of deformation with serrations; v) a final fracturing. Other studies [40,49–51] have pointed out that DSA and the associated serrations occur at the onset of the plastic deformation stage (for strains lower than 0.003) where the twins are far from saturation. In this study, pronounced serrations were already visible at the beginning of plastic deformation and only appeared when the samples were tested at 300 °C and 0.003 s^{-1}. The absence of serrated flows for the higher strain rate and for different temperatures can be attributed to the relationship between dislocation motion and atom diffusion. Particularly, Al addition has been shown to have a strong effect on removing DSA in TWIP steels [30]. The effect of aluminum in TWIP steel is to reduce stacking fault width, which reduces the interaction with the point defect complex leading to a loss of the dynamic pinning [30,52]. This would justify because the examined Fe(C-Mn-Al) TWIP steel does not exhibit serrations in almost all the testing conditions. The appearance of pronounced serrations at 300 °C is attributable to the faster solute mobility that allows moving dislocations to be pinned. However, when TWIP steel was tested at the highest strain rate, the dislocation motion may have been too fast to cause DSA. As discussed previously, DSA is mitigated or disappears at 550 and 800 °C, and, as a consequence, also its macroscopic manifestation (i.e. serrations). Therefore, testing at 300 °C and 0.003 s^{-1} only provides the proper conditions to give rise macroscopic serrations in the examined TWIP steel.

The serrations are often associated with the appearance of narrow mobile deformation bands on the metal surface, which can leave undesirable lines on sheet metal products, with a consequent negative effect on paintability. The presence of banding on the metal surface due to the PLC effect depends on the extent of serrations. The study of Scavino et al. [1] has shown the presence of evident PLC bands on the metal surface of TWIP tensile specimens, which were associated with strong serrations in tensile curves. These serrations were characterized by delta stress over 50 MPa. Differently, the serrations detected in this study are much smaller (delta stress of 5−10 MPa). As a result, the samples with serrations (testing condition: 300 °C and 0.003 s^{-1}) do not exhibit a clear surface banding visible by the naked eye. The slight oxidation on the metal surfaces due to the temperature could also have eliminated possible small traces of PLC banding.

A relationship can be found between serrations and the strain and local strain rate, as may be observed in Figs. 7 and 8, respectively. The serrations in the stress-strain curve correspond to a plateau or to a reduction in the slope of the strain curve. As can be seen in Fig. 7b, during DSA, when dislocations are pinned by a solute and/or C-Mn clusters, stress increases and strain reduces accordingly, due to strengthening.

The local true strain rate was evaluated as the derivative of strain to time. The variation of this factor and tensile stress vs. the engineering strain, in correspondence to serrations, is reported in Fig. 8a. The local strain rate decreases slightly from the onset of the test up to the final fracture, coherently with sample elongation. The occurrence of a serration induces a significant fluctuation in the local strain rate. As shown in Fig. 8b, a macroscopic serration can be anticipated by very small unstable and periodic discontinuities, which reduce the local strain rate by roughly 0.0015 s^{-1}.

A further sudden reduction in the local strain rate occurs in correspondence to the subsequent macroscopic serration. The local strain rate approaches zero, thereby reflecting the occurrence of a DSA mechanism. When serrations are absent, the local strain rate corresponds to the applied strain rate.

The strain hardening rate of TWIP steel was computed as a derivate of the true stress to true strain. The results obtained for the different test conditions are reported in Fig. 9; each of these curves was evaluated up to necking. The strain hardening curves obtained for a low strain rate up to 550 °C show periodic fluctuations, due to the local plastic instability caused by DSA [47,53–57]. When the dislocations pin to interstitial solutes and/or atom clusters, a sharp increase in the resistance to deformation occurs locally, and this is associated with an increase in the strain hardening rate. Once the dislocations have unpinned, a sudden reduction in strength occurs, with an ensuing reduction in the strain hardening rate. Similar successive steps lead to successive fluctuations in the strain hardening curves. The effect of local DSA is particularly clear from the strain hardening rate curves, which are more sensitive to DSA than stress-strain curves (DSA was only detected at 300 °C). Fluctuations were not visible in the samples tested at the highest temperature, that is, 800 °C, and at a high strain rate, thereby confirming the absence of DSA for these testing conditions. In Fig. 9c, the fluctuations are amplified in correspondence to macroscopic serrations (300 °C and 0.003 s^{-1}). This points out a clear correlation between the strain hardening rate curve fluctuations and DSA in TWIP steel.

The strain hardening rate shows an average value of about 3000 MPa in the 0.01-0.03 strain range for the samples tested at 20 and 300 °C. Lower values of about 2000 and 1500 MPa can be

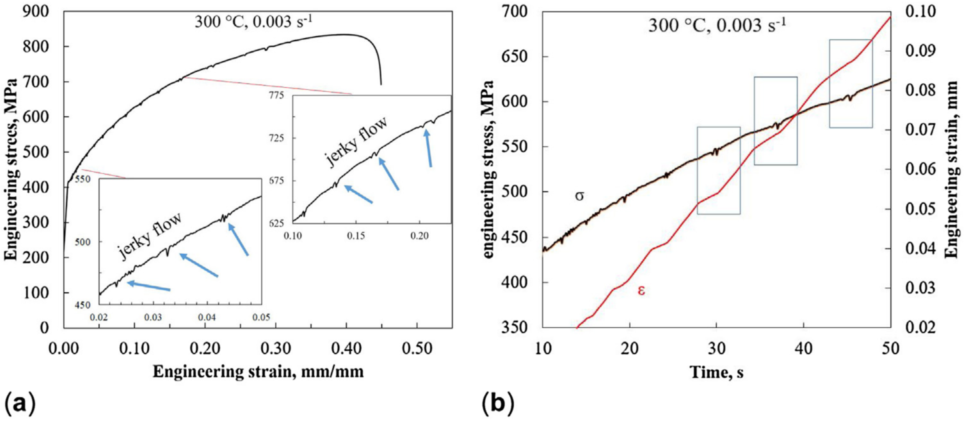

Fig. 7 – Serrations in the a) engineering stress-strain curve and b) their corresponding engineering strain in the 10–50 s time range. Testing condition: 300 °C - 0.003 s^{-1}.

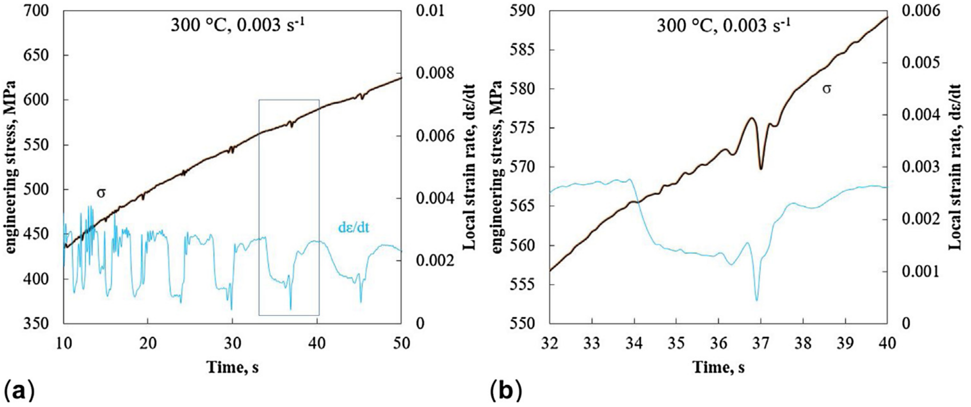

Fig. 8 – a) Example of a local true strain rate evaluated in correspondence to the serrations in the engineering stress-strain curve; b) Inset of image a. Test condition: 300 °C - 0.003 s^{-1}.

detected for the samples tested at 550 and 800 °C, respectively. The strain hardening rate then decreases continuously to the final fracturing, where it exhibits an average value of about half of those obtained at the beginning of the test.

Three main stages can be detected from the strain hardening rate curves of the TWIP steel on the basis of the test conditions. In the first stage, the strain hardening rate reduces steeply with the true strain. In the second stage, the strain hardening rate reduces continuously. The continuous reduction in the strain hardening rate is attributable to the shortening of the mean free path of dislocations, due to the formation of dislocation substructures and deformation twinning [3,58]. Regardless of the occurrence of serrations, the strain hardening rate does not change significantly. It reduces roughly from 3000 to 2000 MPa to the final fracturing. The significant reduction in mechanical twinning at 500 °C leads to an ensuing reduction in strain hardening. At 800 °C, mechanical twinning and DSA are absent, and this leads to a drastic reduction in the strain hardening rate, as can be seen in Fig. 9g. At 800 °C and 0.003 s^{-1}, the predominant effect of recrystallization completely eliminates the capability of TWIP steel to strain harden. This is why there is no image of this testing condition in Fig. 9. The sharp drop in the last stage of the strain rate hardening curves is associated with the final fracturing of the tensile sample (not reported in Fig. 9). A similar plastic flow behavior was also found in previous works [3,59].

3.2. *Microstructures after mechanical testing*

Figs. 10 and 11 display the typical appearance of the deformed microstructure at the border of the gage length closest to the sample ends (i.e. the region subjected to the lowest plastic deformation, zone A in Fig. 2) and to the fracture surface (i.e. the region subjected to the highest plastic deformation, zone B in Fig. 2) obtained from tensile samples. As expected, the grains are notably elongated in the necking region, compared to the more distant regions. Regardless of the strain rate, the microstructures of deformed tensile samples are qualitatively the same at a given temperature. The accommodation of strain by twinning is highlighted by the feathery-shaped substructures, which are indicated with arrows in Figs. 10 and 11. Magnification of these microstructural features is reported in Fig. 12. Similar microstructures have also been reported in other studies [60]. Twins are more visible within grains deformed at 20 and 300 °C, where larger parallel lines appear. Fig. 11 shows that, even though an increase of temperature reduces SFE and hence the occurrence of twinning in the crystal lattice, twinning also occurs at 300 °C. This confirms that

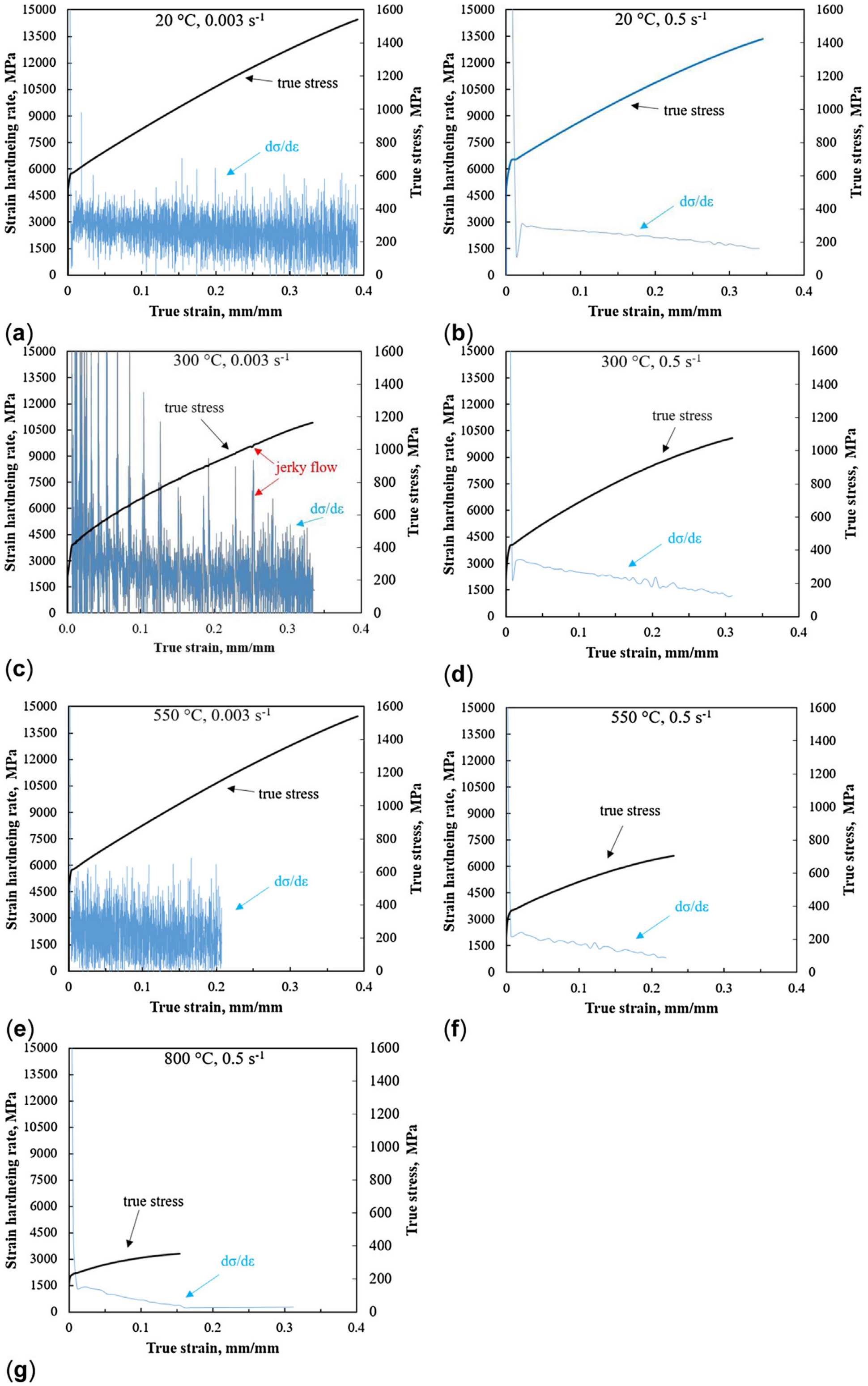

Fig. 9 – Strain hardening rate of TWIP steel: a) 20 °C - 0.003 s^{-1}; b) 20 °C - 0.5 s^{-1}; c) 300 °C - 0.003 s^{-1}; d) 300 °C - 0.5 s^{-1}; e) 500 °C - 0.003 s^{-1}; f) 550 °C - 0.5 s^{-1}; g) 800 °C - 0.5 s^{-1}.

twinning and DSA are the strain hardening mechanisms that contribute to having the highest values of strain hardening exponent in the examined TWIP steel when tested at 300 °C (refer to Fig. 5b). The feathery-shaped substructures are very small and more difficult to distinguish in the samples tested at 500 °C. No deformed grains are visible in the samples tested at 800 °C, due to the significant recrystallization that occurs at this temperature. The few twins that can be seen in these

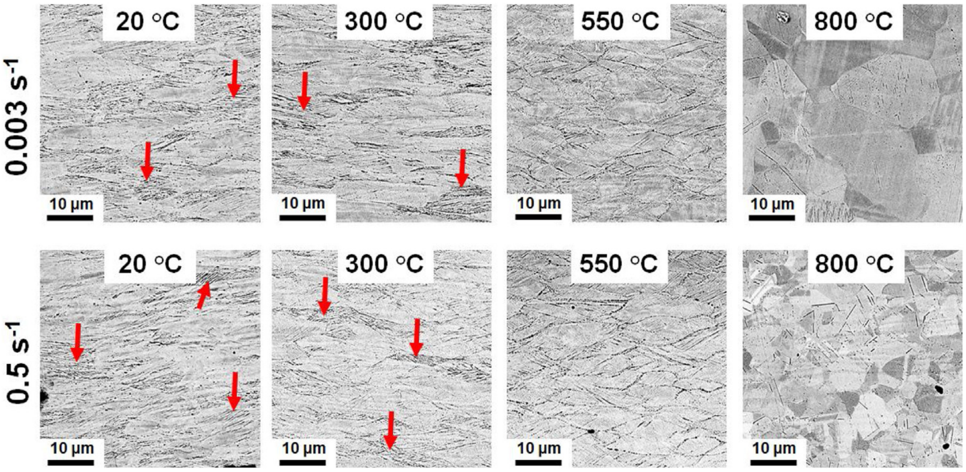

Fig. 10 – Microstructures of the deformed regions close to the necking region for various temperatures and strain rates. The arrows point out some feathery-shaped substructures caused by mechanical twins.

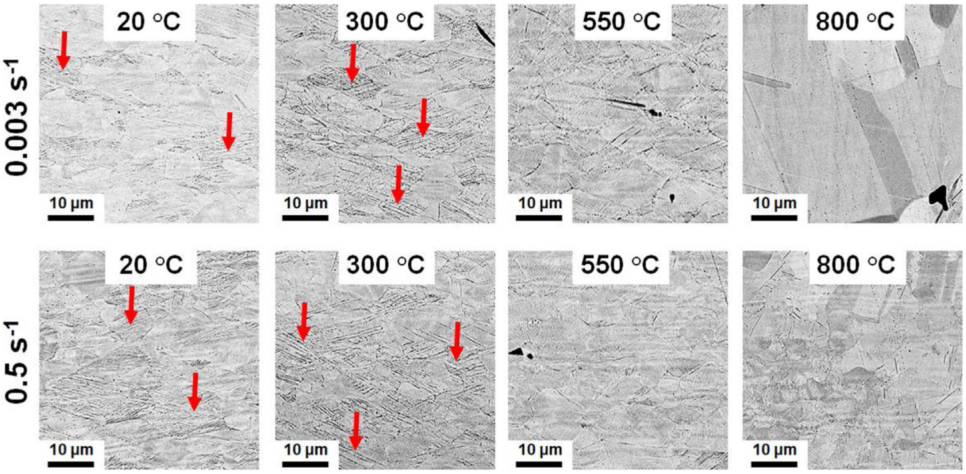

Fig. 11 – Microstructures of the deformed regions at the border of the gage length for various test temperatures and strain rates. The arrows point out some feathery-shaped substructures caused by mechanical twins.

samples are attributable to thermal twins that have originated during grain recrystallization.

3.3. *Fracture surfaces*

The fracture surfaces of the broken tensile samples were examined to assess the fracture modes of TWIP steel under various test conditions. As can be seen in Fig. 13, TWIP steel exhibited the same type of ductile fractures, caused by microvoid coalescence and growth, at 20, 300, and 550 °C, regardless of the strain rate. Deep cavities (highlighted with arrows in Fig. 13) can also be detected. The SEM observation reveals the occurrence of dimples with a somewhat uniform distribution and with a size that increases as the temperature increases. The fracture surfaces do not exhibit dimples at 800 °C. In this case, large cavities are separated by wide metal ligaments, due to the occurrence of creep at high temperatures.

4. Conclusions

The plastic flow behavior of Fe-Mn-C TWIP steel has been investigated during tensile deformation for different temperatures and strain rates. The tensile properties and strain hardening rate of TWIP steel have been addressed in terms of dislocation gliding, twinning, and dynamic strain aging. The following considerations can be made:

- TWIP steel exhibited negative strain rate sensitivity when tested at 20 and 300 °C, which has been associated with a reduction in the ultimate tensile strength as the strain rate increased. This phenomenon disappeared at higher temperatures due to the limited presence (at 550 °C) or absence (at 800 °C) of twinning and DSA mechanisms during plastic deformation.
- DSA, which may be attributed to the Portevin-Le-Chatelier effect, started at the onset of plastic deformation of the sam-

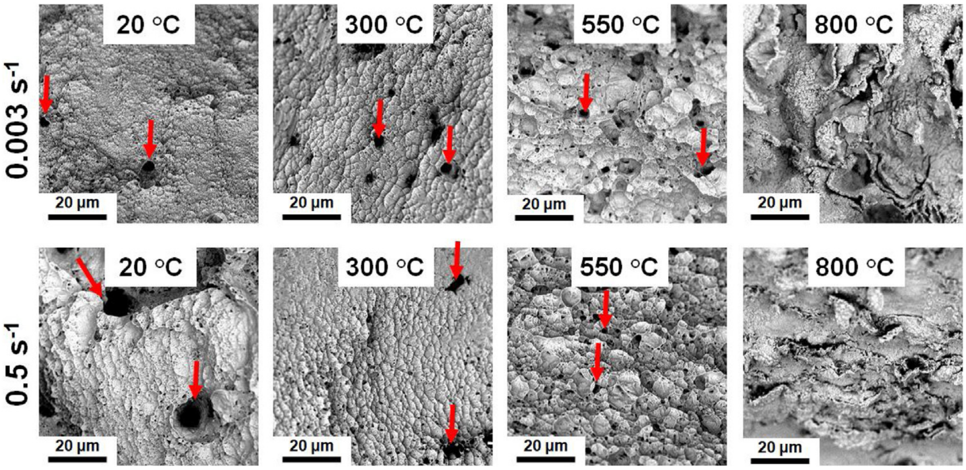

Fig. 13 – Fractographic images of the tensile samples for the various test conditions. The arrows highlight the presence of cavities that occur on the fracture surfaces.

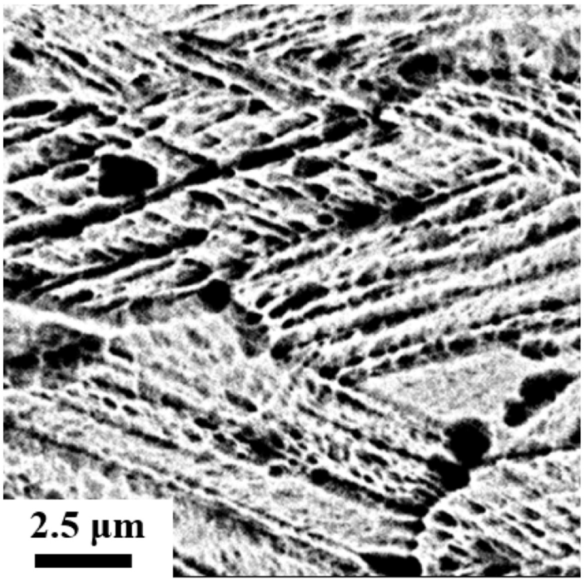

Fig. 12 – Magnification of feathery-shaped substructures caused by the twinning phenomenon.

ples tested at 300 °C and 0.003 s^{-1}. Macroscopic serrations appeared in the corresponding stress-strain curves.

- Regardless of the presence of dislocation gliding, twinning was the main mechanism that promoted the strain hardening of TWIP steel for room to warm temperatures. Under specific conditions (300 °C and 0.003 s^{-1}), DSA improved the strain hardening capability of TWIP steel, by increasing both the strain hardening exponent and the strain hardening rate values.
- Three main stages were detected in the strain hardening rate curves of TWIP steel related to i) a steep reduction of the strain hardening rate; ii) a gradual reduction of the strain hardening rate for most of the test time; iii) a final fracturing.
- The tensile samples showed deformed grains that depended on the extent of plastic deformation. The twins were larger and more visible in the samples tested at 300 °C in a quasi-static condition, where macroscopic stress-strain serrations occurred.
- TWIP steel exhibited a ductile fracture under tensile testing as a result of microvoid coalescence and growth for the sample tested at 20, 300 and 550 °C. Deep cavities separated by wide metal ligaments characterized the fracture surfaces of the sample tested at the highest temperature (800 °C), where creep was an important deformation mechanism.
- TWIP steel exhibited a good mechanical behavior at warm temperatures, as can be seen from the high strength and elongation at fracture values. Therefore, this steel could be successfully used in forming operations at warm temperatures. However, serrations and the appearance of deformation bands on the metal surface may negatively influence the paintability of sheet products made of TWIP steel.
- Since TWIP steel also exhibits noteworthy mechanical properties at higher temperatures than room temperature, stamping of this steel grade at higher temperatures could be a solution to reduce die force involved in stamping operations of car body parts. Although it could be feasible to carry out stamping up to 300 °C, as also demonstrated by the largest strain hardening exponent detected at this temperature, 550 °C and 850 °C are less adequate for stamping of an uncoated TWIP steel due to the oxidation on metal surface and the issues related to the stamping of the metal at such temperatures.

Conflict of interest

The authors declare no conflicts of interest.

REFERENCES

[1] Scavino G, D'aiuto F, Matteis P, Russo Spena P, Firrao D. Plastic localization phenomena in a Mn-alloyed austenitic steel. Metall Mater Trans 2010;41:1493–501, http://dx.doi.org/10.1007/s11661-010-0191-9.

[2] Bouaziz O, Allain S, Scott CP, Cugy P, Barbier D. High manganese austenitic twinning induced plasticity steels: a review of the microstructure properties relationships. Curr Opin Solid State Mater Sci 2011;15:141–68, http://dx.doi.org/10.1016/j.cossms.2011.04.002.

[3] Kusakin PS, Kaibyshev RO. High-Mn twinning induced plasticity steels: microstructure and mechanical properties. Rev Adv Mater Sci 2016;44:326–60. ISSN: 1606-5131.

[4] Pérez Escobar D, Silva Ferreira De Dafé S, Brandão Santos D. Martensite reversion and texture formation in 17Mn-0.06C TRIP/TWIP steel after hot cold rolling and annealing. J Mater Res Technol 2015;4:162–70, http://dx.doi.org/10.1016/j.jmrt.2014.10.004.

[5] Jin JE, Jung YS, Kang S, Lee YK. The effects of Si on the mechanical twinning and strain hardening of Fe–18Mn–0.6C twinning-induced plasticity steel. Acta Mater 2013;61:3399–410, http://dx.doi.org/10.1016/j.actamat.2013.02.031.

[6] Grässel O, Krüger L, Frommeyer G, Meyer LW. High strength Fe-Mn-(Al, Si) TRIP/TWIP steels development - properties – application. Int J Plast 2000;16:1391–409, http://dx.doi.org/10.1016/S0749-6419(00)00015-2.

[7] Mi Zhenli, Di T, Aimin Z, Haitao J. Mechanical properties and microstructure evolution during deformation of Fe–Mn–C TWIP steel. Steel Res Int 2012;83:346–51, http://dx.doi.org/10.1002/srin.201100322.

[8] Hance B. Advanced high-strength steel (AHSS) performance level definitions and targets. SAE Int J Mater Manuf 2018;11:505–16, http://dx.doi.org/10.4271/2018-01-0629.

[9] Ronevich JA, Speer JG, Matlock DK. Hydrogen embrittlement of commercially produced advanced high strength sheet steels. SAE Int J Mater Manuf 2010;3:255–67, http://dx.doi.org/10.4271/2010-01-0447.

[10] Rossini M, Russo Spena P, Cortese L, Matteis P, Firrao D. Investigation on dissimilar laser welding of advanced high strength steel sheets for the automotive industry. Mater Sci Eng A 2015;628:288–96, http://dx.doi.org/10.1016/j.matdes.2016.07.084.

[11] Májlinger K, Kalácska E, Russo Spena P. Gas metal arc welding of dissimilar AHSS sheets. Mater Des 2016;109:615–21, http://dx.doi.org/10.1016/j.msea.2015.01.037.

[12] Russo Spena P, Matteis P, Scavino G. Dissimilar metal active gas welding of TWIP and DP steel sheets. Steel Res Int 2015;86:495–501, http://dx.doi.org/10.1002/srin.201400154.

[13] Russo Spena P, De Maddis M, Lombardi F, Rossini M. Dissimilar resistance spot welding of Q&P and TWIP steel sheets. Mater Manuf Proc 2016;31:291–9, http://dx.doi.org/10.1080/10426914.2015.1048476.

[14] Russo Spena P, Cortese L, Nalli F, Májlinger K. Local formability and strength of TWIP-TRIP weldments for stamping tailor welded blanks (TWBs). Int J Adv Manuf Technol 2019;101:757–71, http://dx.doi.org/10.1007/s00170-018-2946-1.

[15] Halbauer L, Zenker R, Weidner A, Buchwalder A, Biermann H. Electron beam welding of cold rolled high-alloy TRIP/TWIP steel sheets. Steel Res Int 2016;87:436–44, http://dx.doi.org/10.1002/srin.201500086.

[16] Savic V, Hector L, Singh H, Paramasuwom M, Basu U, Basudha A, et al. Development of a lightweight third-generation advanced high-strength steel (3GAHSS) vehicle body structure. SAE Int J Mater Manuf 2018;11:303–11, http://dx.doi.org/10.4271/2018-01-1026.

[17] Li D, Wei Y, Liu C, Hou L. Hot deformation behaviors of Fe–30Mn–3Si–3Al TWIP steel during compression at elevated temperature and strain rate. Steel Res Int 2013;84:740–50, http://dx.doi.org/10.1002/srin.201200254.

[18] Shen Y, Qiu C, Zhang R, Xue W, Liu Y. Tensile properties of a Fe-20Mn-3Si-3Al-0.045C steel at different strain rates and various temperatures. In: Proceedings of the 14th International Conference on Metal Forming, METAL FORMING 2012. 2012. p. 1179–82.

[19] Lee S, De Cooman BC. Annealing temperature dependence of the tensile behavior of 10 pct Mn multi-phase TWIP-TRIP steel. Metall Mater Trans 2014;45:6039–52, http://dx.doi.org/10.1007/s11661-014-2540-6.

[20] Frank FC, Read WT Jr. Multiplication processes for slow moving dislocations. Phys Rev 1950;79:722–3, http://dx.doi.org/10.1103/PhysRev.79.722.

[21] Orowan E. Fracture and strength of solids. Rep Prog Phys 1949;12:185–232, http://dx.doi.org/10.1088/0034-4885/12/1/309.

[22] Bouaziz O, Guelton N. Modelling of TWIP effect on work hardening. Mater Sci Eng A 2001;319–321:246–9.

[23] Huang BX, Wang XD, Rong YH, Wang L, Jin L. Mechanical behavior and martensitic transformation of an Fe–Mn–Si–Al–Nb alloy. Mater Sci Eng A 2006;438–440:306–11.

[24] Pierce DT, Jiménez JA, Bentley J, Raabe D, Wittig JE. The influence of stacking fault energy on the microstructural and strain-hardening evolution of Fe–Mn–Al–Si steels during tensile deformation. Acta Mater 2015;100:178–90, http://dx.doi.org/10.1016/j.actamat.2015.08.030.

[25] Allain S, Chateau JP, Bouaziz O, Migot S, Guelton N. Correlations between the calculated stacking fault energy and the plasticity mechanisms in Fe–Mn–C alloys. Mater Sci Eng A 2004;158:387–9, http://dx.doi.org/10.1016/j.msea.2004.01.059.

[26] Curtze S, Kuokkala VT. Dependence of tensile deformation behavior of TWIP steels on stacking fault energy, temperature and strain rate. Acta Mater 2010;58:5129–41, http://dx.doi.org/10.1016/j.actamat.2010.05.049.

[27] Pierce DT, Jimenez JA, Bentley J, Raabe D, Oskay C, Wittig JE. The influence of manganese content on the stacking fault and austenite/ε-Martensite interfacial energies in Fe–Mn–(Al–Si) steels investigated by experiment and theory. Acta Mater 2014;68:238–53, http://dx.doi.org/10.1016/j.actamat.2014.01.001.

[28] Grässel O, Frommeyer G, Derder C, Hofmann H. Phase transformations and mechanical properties of Fe–Mn–Si–Al TRIP-Steels. J Phys Iv 1997;7. C5-383-C5-388. ISSN: 1155-4339.

[29] Dumay A, Chateau JP, Allai S, Migot S, Bouaziz O. Influence of addition elements on the stacking-fault energy and mechanical properties of an austenitic Fe–Mn–C steel. Mater Sci Eng A 2008;483–484:184–7, http://dx.doi.org/10.1016/j.msea.2006.12.170.

[30] Kim J, Lee SJ, De Cooman BC. Effect of Al on the stacking fault energy of Fe–18Mn–0.6C twinning-induced plasticity. Scripta Mater 2011;65:363–6, http://dx.doi.org/10.1016/j.scriptamat.2011.05.014.

[31] Christian JW, Mahajan S. Deformation twinning. Prog Mater Sci 1995;39:1–157, http://dx.doi.org/10.1016/0079-6425(94)00007-7.

[32] Rose KSB, Glover SG. A study of strain-ageing in austenite. Acta Metall 1966;14:1505–16.

[33] Chen L, Kim HS, Kim SK, De Cooman BC. Localized deformation due to portevin-le-Chatelier effect in 18Mn-0.6C TWIP austenitic steel. ISIJ Int 2007;47:1804–2812, http://dx.doi.org/10.2355/isijinternational.47.1804.

[34] Zaiser M, Hahner P. Multiple features in electronic raman spectra of HgBa2Ca2Cu3O8. Phys Status Solidi B 1997;199:267–330.

[35] Cuddy LJ, Leslie WC. Some aspects of serrated yielding in substitutional solid solutions of iron. Acta Metall 1972;20:1157–67, http://dx.doi.org/10.1016/0001-6160(72)90164-2.

[36] Dastur YN, Leslie WC. Mechanism of work hardening in Hadfield manganese steel. Metall Trans A 1981;12:749–59.

[37] ASTM E8. Standard test methods for tension testing of metallic materials. ASTM International; 2016.

[38] ASTM E21. Standard test methods for elevated temperature tension testing of metallic materials. ASTM International; 2017.

[39] ASTM E646. Standard test method for tensile strain-hardening exponents (n -Values) of metallic sheet materials. ASTM International; 2016.

[40] Lan P, Zhang J. Twinning and dynamic strain aging behavior during tensile deformation of Fe-Mn-C TWIP steel. Mater Sci Eng A 2017;700:250–8, http://dx.doi.org/10.1016/j.msea.2017.06.012.

[41] Lan P, Du C, Ji Y. Research status of high manganese TWIP steel for automotive industry. China Metall 2014;24:6–16.

[42] Lan P. Analysis of solidification characteristics and structure performance on TWIP steels for automotive, doctoral dissertation. Beijing: University of Science and Technology; 2015.

[43] Madivala M, Bleck W. Strain rate dependent mechanical properties of TWIP steel. Adv High-Strength Steel Automob 2019;71:1291–302, http://dx.doi.org/10.1007/s11837-018-3137-0.

[44] Lee SJ, Kim J, Kane SN, De Cooman BC. On the origin of dynamic strain aging in twinning-induced plasticity steels. Acta Mater 2011;59:6809–19, http://dx.doi.org/10.1016/j.actamat.2011.07.040.

[45] Renard K, Ryelandt S, Jacques PJ. Characterisation of the portevin-le-Chatelier effect affecting an austenitic TWIP steel based on digital image correlation. Mater Sci Eng A 2010;527:2969–77, http://dx.doi.org/10.1016/j.msea.2010.01.037.

[46] Saeed-Akbari A, Mishra AK, Mayer J, Bleck W. Characterization and prediction of flow behavior in high-manganese twinning induced plasticity steels: part II. Jerky flow and instantaneous strain rate. Metall Mater Trans 2012;43:1705–23, http://dx.doi.org/10.1007/s11661-011-1070-8.

[47] Lebedkina TA, Lebyodkin MA, Chateau JP, Jacques A, Allain S. On the mechanism of unstable plastic flow in an austenitic FeMnC TWIP steel. Mater Sci Eng A 2009;519:147–54, http://dx.doi.org/10.1016/j.msea.2009.04.067.

[48] Saeed-Akbari A, Mishra AK, Mayer J, Bleck W. Characterization and prediction of flow behavior in high-manganese twinning induced plasticity steels: part II. Jerky flow and instantaneous strain rate. Metall Mater Trans A 2012;43:1705–23.

[49] Hong S, Shin SY, Lee J, Ahn DH, Kim HS, Kim SK, et al. Serration phenomena occurring during tensile tests of three high-manganese twinning-induced plasticity (TWIP) steels. Metall Mater Trans A 2014;45:633–46.

[50] Koyama M, Sawaguchi T, Lee T, Lee CS, Tsuzaki K. Work hardening associated with ε-martensitic transformation, deformation twinning and dynamic strain aging in Fe–17Mn–0.6C and Fe–17Mn–0.8 C TWIP steels. Mater Sci Eng A 2011;528:7310–6.

[51] Renard K, Ryelandt S, Jacques PJ. Characterisation of the Portevin-Le Châtelier effect affecting an austenitic TWIP steel based on digital image correlation. Mater Sci Eng A 2010;527:2969–77.

[52] Park KT, Jin KG, Han SH, Hwang SW, Choi K, Lee CS. Stacking fault energy and plastic deformation of fully austenitic high manganese steels: effect of Al addition. Mater Sci Eng A 2010;527:3651–61.

[53] Chen L, Kim HS, Kim SK, De Cooman BC. Localized deformation due to Portevin–LeChatelier effect in 18Mn–0.6 C TWIP austenitic steel. ISIJ Int 2007;47:1804–12.

[54] Zavattieri PD, Savic V, Hector LG, Fekete JR, Tong W, Xuan Y. Spatio-temporal characteristics of the Portevin–Le Châtelier effect in austenitic steel with twinning induced plasticity. Int J Plast 2009;25:2298–330.

[55] Lee SJ, Kim J, Kane SN, De Cooman BC. On the origin of dynamic strain aging in twinning induced plasticity steels. Acta Mater 2011;59:6809–19.

[56] Kim JK, De Cooman BC. Stacking fault energy and deformation mechanisms in Fe-xMn-0.6C-yAl TWIP steel. Mater Sci Eng A 2016;676:216–31.

[57] Saeed-Akbari A, Mosecker L, Schwedt A, Bleck W. Characterization and prediction of flow behavior in high-manganese twinning induced plasticity steels: part I. Mechanism maps and work-hardening behavior. Metall Mater Trans A 2012;43:1688–704.

[58] Gutierrez-Urrutia I, Raabe D. Dislocation and twin substructure evolution during strain hardening of an Fe–22 wt.% Mn–0.6 wt.% C TWIP steel observed by electron channeling contrast imaging. Acta Mater 2011;59:6449–62, http://dx.doi.org/10.1016/j.actamat.2011.07.009.

[59] Yang HK, Zhang ZJ, Zhang ZF. Comparison of twinning evolution with work hardening ability in twinning-induced plasticity steel under different strain rates. Mater Sci Eng A 2015;622:184–8, http://dx.doi.org/10.1016/j.msea.2014.11.031.

[60] Benzing JT, Poling WA, Pierce DT, Bentley J, Findley KO, Raabe D, et al. Effects of strain rate on mechanical properties and deformation behavior of an austenitic Fe-25Mn-3Al-3Si TWIP-TRIP steel. Mater Sci Eng A 2018;711:78–92, http://dx.doi.org/10.1016/j.msea.2017.11.017.